IEEE Photonics Journal
An IEEE Photonics Society Publication

Open Access

A Holography-Based Modal Wavefront Sensor for the Precise Positioning of a Light Emitter Using a High-Resolution Computer-Generated Hologram

Volume 10, Number 1, February 2018

Florian Loosen
Johannes Stehr
Lucas Alber
Irina Harder
Norbert Lindlein

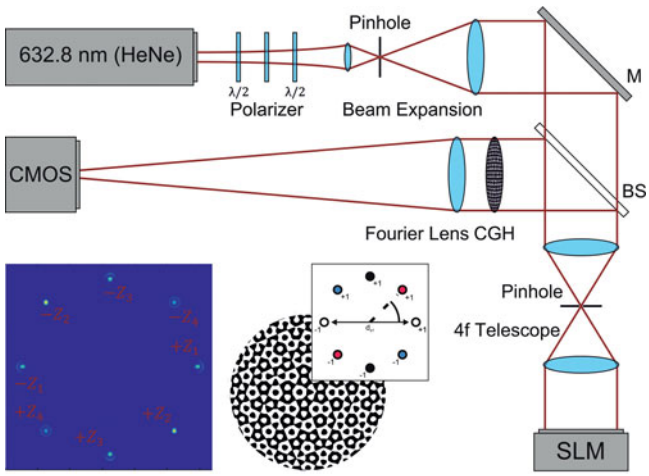

DOI: 10.1109/JPHOT.2018.2799383
1943-0655

IEEE photonics SOCIETY
IEEE

A Holography-Based Modal Wavefront Sensor for the Precise Positioning of a Light Emitter Using a High-Resolution Computer-Generated Hologram

Florian Loosen,[1] **Johannes Stehr**,[1] **Lucas Alber**,[1,2] **Irina Harder**,[2] **and Norbert Lindlein** [1]

[1]Institute of Optics, Information and Photonics, Friedrich-Alexander-Universität Erlangen-Nürnberg, Erlangen 91058, Germany
[2]Max Planck Institute for the Science of Light, Erlangen 91058, Germany

DOI:10.1109/JPHOT.2018.2799383

Manuscript received December 11, 2017; revised January 15, 2018; accepted January 24, 2018. Date of publication January 31, 2018; date of current version February 19, 2018. Corresponding author: Florian Loosen (e-mail: florian.loosen@fau.de).

Abstract: In certain applications, modal wavefront sensors (MWFSs) can outperform zonal wavefront sensors, which are widely used due to their high flexibility. In this paper, a holography-based MWFS as described is developed for the fast position control of a light emitter in a deep parabolic mirror. The light source is located in the vicinity of the focal point. Instead of Zernike polynomials, more complex phase functions, which are related to certain dislocations of the light source are used as detector modes. The performance of the sensor is verified with a test setup, where the test wavefront is generated by a spatial light modulator instead of a real parabolic mirror. The design and fabrication of the required high-resolution holographic element is described and an easy way of multiplexing several single mode sensors is demonstrated.

Index Terms: Advanced optics design, diffractive optics, holography.

1. Introduction

The established method for measuring the wavefront of a light wave is the measurement of the spatial phase distribution, e.g. with a Shack-Hartmann Sensor (SHS) [1], [2] or other Wavefront Sensor (WFS) concepts [3]. For the SHS, a modal wavefront representation is often described via polynomials (such as a series of Zernike polynomials) by fitting the measured point deviations at the sample points to the partial derivatives of these polynomials. Under certain conditions, a direct measurement of the individual modal components of the phase function can be beneficial to measure the wavefront of a definite system (see Fig 1). This modal method can greatly simplify the complexity of data processing and may increase the measuring speed. The main element of the modal sensor, presented in this work, is a Computer-Generated Hologram (CGH) [4]. This element carries the phase function modes (based on Zernike polynomials [5] or any linear combination) in the order of magnitude of the aberrations to be measured. In principle, the measurement method can be described as the reconstruction of a plane object wave by a specifically aberrated reference wavefront (disturbed by aberrations in a particular system) [6]. The intensity distribution thus created in the focal plane of a lens carries all information about this disturbance [7]. To motivate the use of

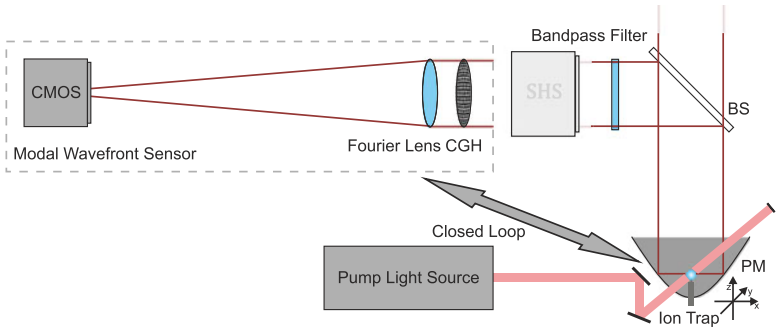

Fig. 1. Setup with a Shack-Hartmann Sensor (SHS) to measure the wavefront which is produced by collimating the light of a fluorescent ion with a Parabolic Mirror (PM) [8]. With a MWFS instead of a SHS, a closed loop can be established to position the ion in the focal point of the PM [12].

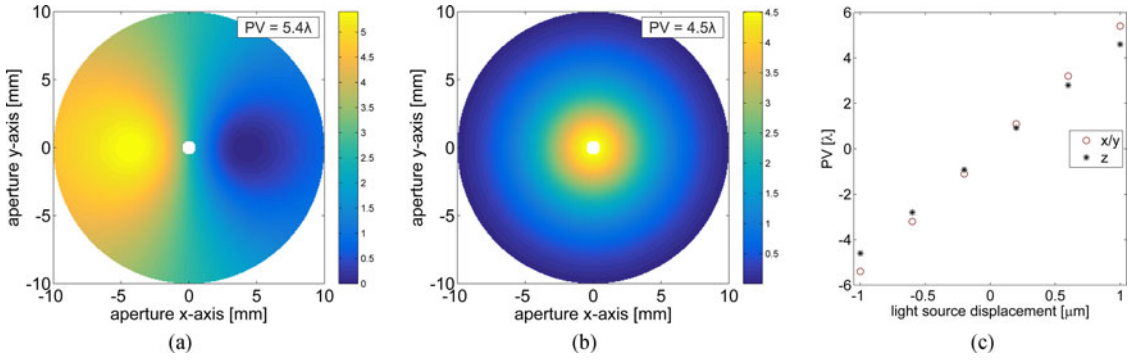

Fig. 2. (a) and (b) represent the simulated phase functions, resulting from lateral and axial light source displacements and (c) the linear dependence of the aberration magnitude on the displacement. The non-defined area in the middle is due to a hole in the mirror at the vertex which is necessary to mount the ion trap.

a MWFS, a part of the setup explained in [8] is shown in Fig. 1 with some changes. A fluorescent ion is trapped in a deep Parabolic Mirror (PM). The exact positioning of the ion at the focal point of the PM [9] is challenging under the conditions present in the respective experiment. A promising technique to achieve fast and precise aligning is the use of a holography based MWFS to establish e.g. a closed loop position contol. The quantitative investigation of such a MWFS is presented in the following chapters. Up to now, most articles (e.g. [10], [11]) concern the principal function of the sensing in simulation and basic measurements. The work descirbed in this article includes a different design, simulation, and fabrication method as well as a “more” complex application for the MWFS.

2. Relevant Aberration Modes

To determine the aberration modes which are relevant in the context of the application described, the parabolic mirror system was simulated with the IOIP’s in-house developed ray-tracing software RAYTRACE. A point source ($\lambda = 370$ nm) is located at the focal point of the parabolic mirror which has a focal length of 2.1 mm and an aperture diameter of 20 mm. It thereby covers nearly the full 4π solid angle around the focus. Fig. 2 shows the phase (de-adjustment modes) in the mirror aperture for a light source displacement of 1 μm in (a) lateral (x- and y-direction have equal effects but rotated by 90°) and (b) axial displacement. A fit of Zernike polynomials reveals that the dominating Zernike modes are primary coma and tilt for a lateral displacement and defocus and primary spherical aberration for a displacement in axial direction. It can be shown that both, the

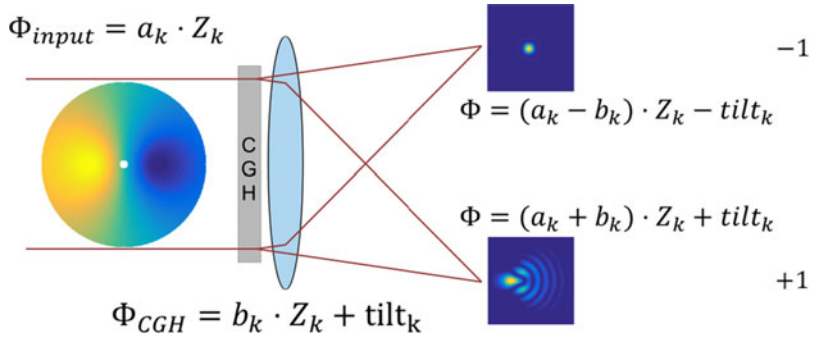

Fig. 3. Functional principle of a modal wavefront sensor for measuring a specific mode distribution (here lateral shift of the ion in x-direction). This is based on the separation of the modes into the ±1st diffraction orders. The principle setup includes an incoming wavefront, the CGH structure, and a Fourier lens for imaging. [14]

coefficients of the Zernike modes and the phase Peak-to-Valley (PV) values are proportional to the displacement of the light source [see Fig. 2(c)]. The phase functions related to different directions of displacement show no significant overlays. Subsequently, a sensor which can be used in a closed loop ion position control has to be sensitive to one mode per spatial direction. By measuring the wavefront deformation characterized by the described modes, it is possible to deduce the position of the point emitter in the system.

3. Sensor Principle

The fundamental principle of the sensor is based on a holographic element which transforms a specifically aberrated wavefront into a tilted plane wave. The holographic element is realized as CGH which should have a $+1$st as well as a -1st diffraction order. If the incoming wave (object wave) carries the same mode as the one which is encoded in the CGH structure, the aberration mode will be amplified in one diffraction order as well as impaired in another. A CGH with a strong $+1$st and -1st diffraction order (each about 40%) can be realized with a simple binary element which also simplifies the fabrication compared to blazed elements. Furthermore, a binary CGH can be designed such that the even diffraction orders are suppressed. A sensor of this type was proposed in [7]. The aberrated input wavefront, whose phase function $\Phi_{in} = \sum_k a_k Z_k$ is regarded as a set of aberration modes Z_k, is given an additional phase $\Phi_{CGH_l} = b_l Z_l$ by the CGH which represents a single mode Z_l. For $l = k$, the coefficient a_k can be determined. In the nth diffraction order, the resulting phase front for a certain aberration mode Z_k can be represented as:

$$(a_k \pm n \cdot b_k) \cdot Z_k. \tag{1}$$

In the example shown in Fig. 3, the measurement of the parabolic mirror mode in x-direction is sketched for the special case where $a_k = b_k$. In the -1st diffraction order, the wavefront error of the incoming wavefront is completely compensated by the added phase of the CGH. The result is an aberration-free Point Spread Function (PSF) in the focal plane of the Fourier lens [13]. In the $+1$st diffraction order the phase aberration of the incoming wave is doubled at the CGH. Hence, the PSF shows significant distortions (primary coma and tilt). In addition, a tilt is intentionally added so that the spot in the focal plane of the Fourier lens is located at a well-defined off-axis position. The intensity in the respective diffraction orders can be represented as:

$$I_\pm \propto |\mathscr{F}\{\exp[i((a_k \pm b_k) \cdot Z_k \pm tilt_k)]\}|^2. \tag{2}$$

Fig. 4 shows exemplary intensity distributions of primary coma in the ±1st diffraction orders. In order to evaluate the intensity distribution in the focal plane of the Fourier lens and to obtain a measuring signal, the optical powers in the ±1st diffraction orders are measured [see Fig. 5(a)]. The active area of the used detectors have the size of the Airy disc. The sensor output signal

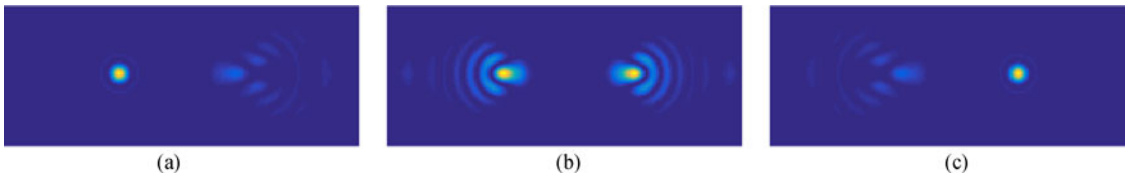

Fig. 4. Intensity distribution in the ±1st diffraction orders (intensity distribution in the detector plane) (a) for $a = b$, (b) $a = 0$, and (c) $a = -b$. The mode that is visualized is primary coma in x-direction.

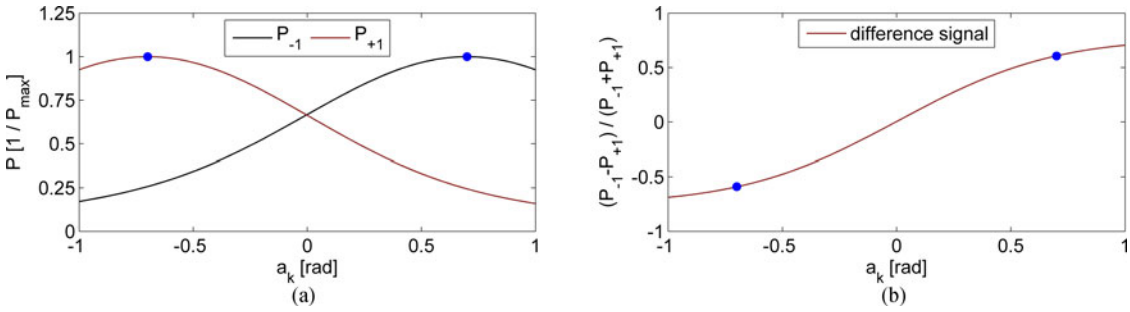

Fig. 5. (a) Comparison of the powers P (normalized) of the simulated measurement signals from Fig. 3, whereby the magnitude of the incoming wavefront error a_k is varied. (b) Normalized difference signal S of the power values inside the defined apertures (point detectors). The phase amplitude of the aberration imprinted into the CGH is 0.7 rad (blue dots).

S is obtained as the normalized difference value ($S = \frac{P_{+1}-P_{-1}}{P_{+1}+P_{-1}}$) of the optical powers in the ±1st diffraction orders [see Fig. 5(b)]. [15]

As described before, the radii of the two detectors are chosen such that the PSF of the aberration-free wavefront up to its first intensity minimum is completely located in the pinhole. By using pixel-based detectors, however, other possibilities as in [16] can be useful.

4. Design and Fabrication

The structure of the holographic sensor element for a single mode wavefront sensor can be calculated from (3). It represents the interference pattern of an aberrated reference wavefront $u_{ref} \propto \exp[ib_k Z_k]$ with a plane tilted object wavefront $u_{obj} \propto \exp[i\tau_k]$, where τ_k represents the tilt function.

$$CGH_k = 2 + 2 \cdot \cos(b_k Z_k - \tau_k) \tag{3}$$

By binarizing the results of (3), the diffraction efficiencies for the +1st and −1st order can be optimized while the even diffraction orders can be suppressed. For a multimodal wavefront sensor the results of (3) for different aberration modes can be summed up before binarizing. It can be shown that after binarization the resulting multiplexed CGH is equivalent to a CGH which was obtained by first adding the complex amplitudes $u_k \propto \exp[i(b_k Z_k + \tau_k)]$ and then encoding only the binarized phase of the resulting complex function. The diffraction orders of different single mode holograms can be separated spatially by rotating the tilt function, as illustrated in Fig. 6. If the CGH is illuminated with a plane (aberration-free) wavefront, the PSFs shown in Fig. 9(a) are generated in the ±1st diffraction orders. For the presented experiments, the sensor modes were chosen to be the simulated phase functions of the parabolic mirror. For Zernike mode sensors Neil *et al.* propose maximal sensor sensitivity for a bias Zernike magnitude of around 0.7 rad [7]. For the definition of primary coma as used by Neil *et al.* this corresponds to a PV value of 2.8 rad. As a trade of, the highest measurable ion displacement, which is defined by the sensor bias aberration, was chosen to be ±160 nm. This corresponds to bias magnitudes between 4.5 rad (PV) and 5.4 rad (PV). The

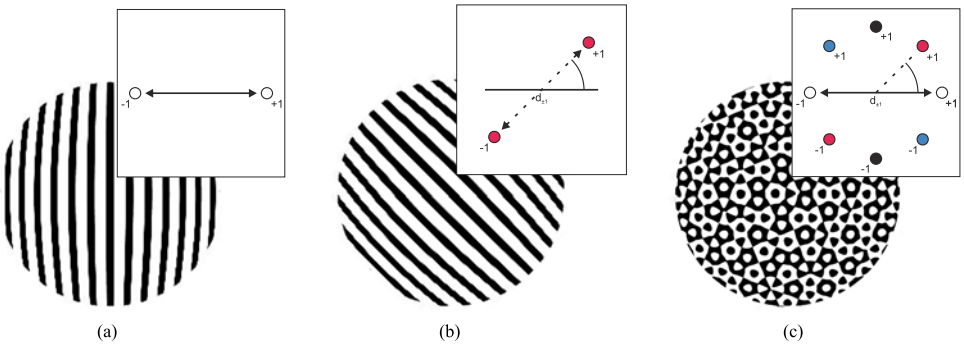

Fig. 6. Phase-structure of single mode detectors with tilt functions rotated by (a) 0° and (b) 45°. (c) shows the summed CGH structure of 4 single detectors arranged around 360°. Each box shows the sensor arrangement at the detector (image surface). The various color points represent different sensor elements to measure the defined modes.

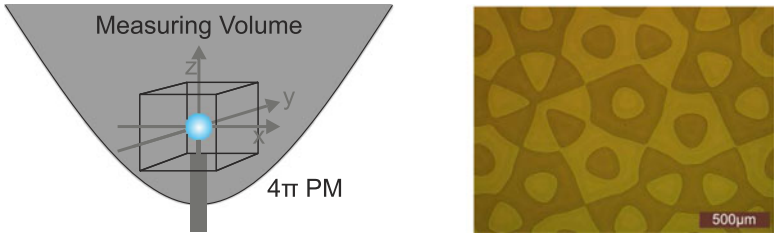

Fig. 7. (a) Measuring volume of the Modal Wavefront Sensor (MWFS) in the 4π PM. For the sensor presented, the highest measurable ion displacement was chosen to be ± 160 nm. (b) Microscope image of the CGH structure.

resulting measuring volume is illustrated in Fig. 7(a). The tilt function was chosen in a way, that the $\pm$1st diffraction orders had a separation of 2 mm at a working distance of 1000 mm.

The fabrication of the CGH structure was done in a 3 steps production process. In the first step, the substrate was cleaned and prepared for the subsequent steps. The chromium-coated fused silica [17] wafer was spin coated with a photoresist (*AZ MIR 701/MicroChemicals GmbH*). After this, the designed CGH was written into the photoresist using direct laser writing. The writer (*DWL66+/Heidelberg Instruments GmbH*) has a maximum resolution of 100 nm. The binary structure has a pixel resolution of 200 nm, resulting from the CGH design diameter and the number of pixels. For the test setup, shown in Fig. 8, the CGH diameter was required to be 8.64 mm. Hence the CGH was fabricated with a resolution of $43,200$ pixel $\times$ $43,200$ pixel. After a development process of the exposed resist layer the CGH structure was transferred to the chromium layer by a wet etching process. As final step, the wafer was etched using reactive ion etching (*Plasmalab System 100/Oxford Instruments plc*). The plasma was composed of 45 sccm of CF_4 and 5 sccm of H_2. The entire process was accompanied by pre- and post-exposure bake units and finished by a lift off to remove all remnants of chromium and resist. A microscope image of the produced CGH structure is shown in Fig. 7(b). The final structure height was $h = (650 \pm 2)$ nm which deviates from the optimal value of $h = 692$ nm by 6%.

5. Experimental Setup

In order to demonstrate the course of the sensory-type difference signal S [11], a modal wavefront sensor system for the de-adjustment modes Z_1 to Z_4 was realized and characterized by a test setup. Here, Z_1 represents the mode for displacement along the lateral x-axis, Z_2 the mode with a plane

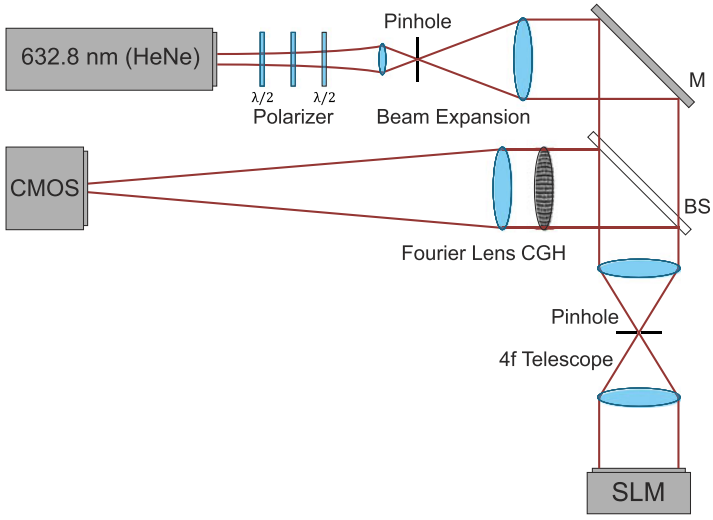

Fig. 8. Experimental setup for verifying the functional principle of a modal wavefront sensor. The setup includes a laser beam source which is linearly polarized and expanded to a homogeneous plane wave. A Mirror (M) and a Beam Splitter (BS) to realize a compact experimental setup. In addition, the BS is used since the Spatial Light Modulator (SLM) works in reflection and the 4*f* telescope with a pinhole allows to filter out unwanted diffraction orders of the SLM. Then, the actual modal wavefront sensor consists of a CGH with the imprinted reference signal and a Fourier lens for focusing the PSFs onto the image plane and a CMOS camera for recording.

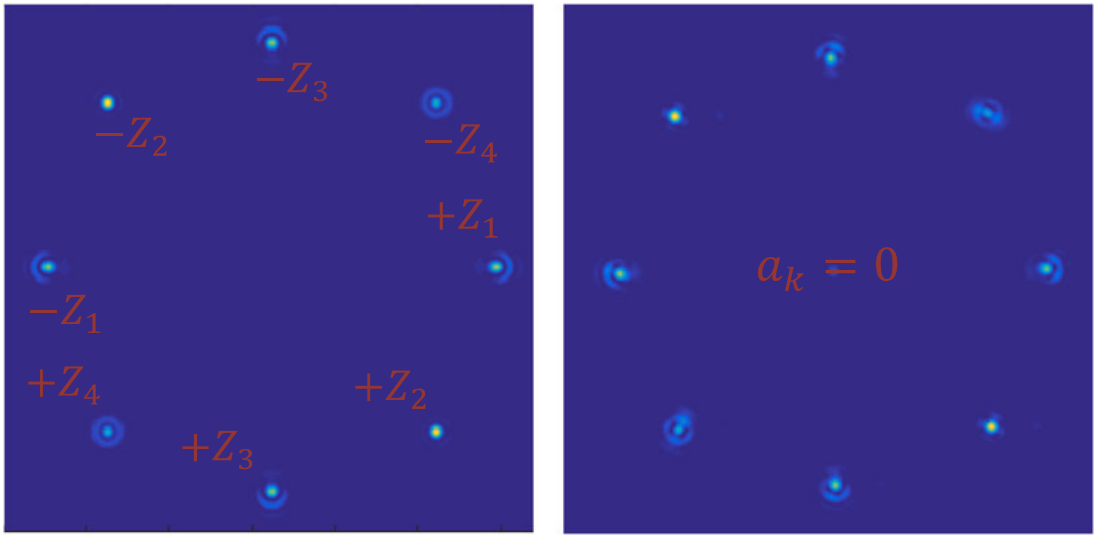

Fig. 9. (a) Simulated intensity distribution in the focal plane of the sensor. Z_1, Z_2, Z_3, and Z_4 represents the phase functions of four different modes in the $\pm$1st diffraction orders. (b) shows the measured detector signal. In the experiment as well as in the simulation a plane test wavefront ($a_k = 0$) impinges onto the sensor.

wavefront as reference, Z_3 the mode for displacement along the lateral y-axis, and Z_4 the mode for shifts in axial direction. The exact sensor arrangement in simulation and experiment is shown in Fig. 9(a) and (b). Fig. 8 shows a basic sketch of the experimental setup that verifies the functional principle of the modal wavefront sensor. The experimental setup includes a laser beam source ($\lambda = 632.8$ nm) which is linearly polarized by a polarizer. A telescope (beam expander) expands the diameter of the laser so that the incident wavefront is a homogeneous plane wave. Thereby, the

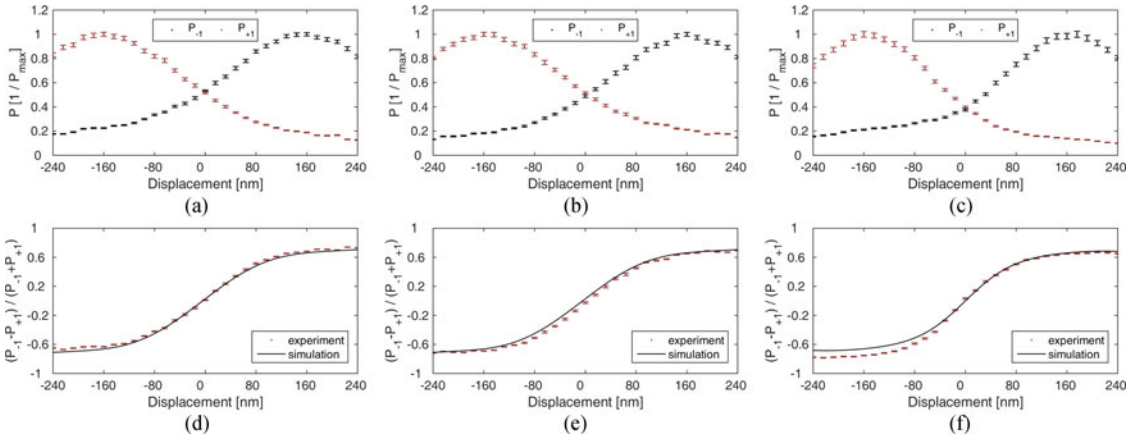

Fig. 10. Comparison of the simulated and measured powers P in the pinholes (a)–(c) and the normalized differences of the sensor output signals S at the detector plane (d)–(f) for all three mirror modes (Z_1, Z_3, and Z_4).

beam is over-expanded to ensure homogeneous illumination at the Spatial Light Modulator (SLM) (*PLUTO-VIS-014/HOLOEYE Photonics AG*). A Mirror (M) folds the beam path. A Beam Splitter (BS) is necessary since the SLM works in reflection and the 4f telescope with a pinhole allows to filter out unwanted diffraction orders of the SLM. Of course, the size of the pinhole has to be adapted to the aberration which is generated by the SLM. Then, the actual modal wavefront sensor consists of a CGH with the imprinted reference signal and a Fourier lens for focusing the PSFs onto the image plane and a CMOS camera for recording. Fig. 9 displays the intensity distribution in the focal plane of the Fourier lens generated by the CGH structure (opposite PSFs show the same aberration but with the $\pm$1st diffraction orders of the CGH) in (a) as simulation and (b) as experimental result.

6. Measurement and Data Processing

For the test of the sensor principle, the SLM was used to prepare a test wavefront according to a certain position of the ion in the PM. The sensor response was evaluated for 41 virtual ion positions in the range of $[-240\ \text{nm},\ 240\ \text{nm}]$ per spatial direction. All measurements were performed several times to obtain the statistic variations and to prove the reproducibility of the sensor output. The intensity distribution in the Fourier plane of the lens was mapped by a CMOS camera and evaluated in MATLAB. To determine the ideal position for the evaluation, a Gaussian function (a Bessel function of the first kind [18] is also possible) was fitted to the aberration-free focal spots ($a_k = \pm b_k$). The "virtual pinhole radius", i.e. the pixel area on the CMOS camera which is evaluated for one spot, was chosen to be the size of the Airy disc $r_{Airy} = 89\ \mu$m. For the experiments, the test wavefront was aberrated by one mirror mode and the responses of the corresponding diffraction orders were investigated. In Fig. 10 the optical powers measured in the pinholes ((a)–(c)) and the resulting sensor responses ((d)–(f)) for all three mirror modes (Z_1, Z_3, and Z_4) are shown. The given errors denote the standard deviations obtained from ten independent measurements. It can be seen that the statistical variations of the measured optical powers are significantly higher than the variations of the sensor output. This can be explained, since all effects with equal impact on both diffraction orders vanish at the difference signal operation. Hence, the resulting response curves are highly reproducible and can therefore be used as calibration curves. Furthermore, the measured sensor responses are in good accordance with simulative results, proving the predictability of this sensing method. It can also be seen, that systematic effects can cause reproducible deviations between simulative and experimental results. Those systematic errors have to be taken into account while a calibration of the sensor. Since systematic effects are related to a certain setup, this reveals a weak point of modal wavefront sensing. In order to achieve reliable measurement results all sources of

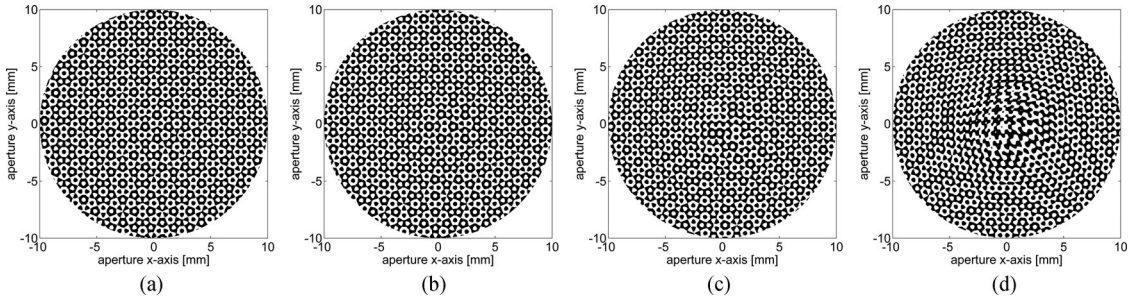

Fig. 11. The strength of the related phase function depends strongly on the defined measuring range or more specifically the measuring volume. (a)–(d) display the CGH structures for measurement volumes with a half edge length from 80 nm to 1000 nm.

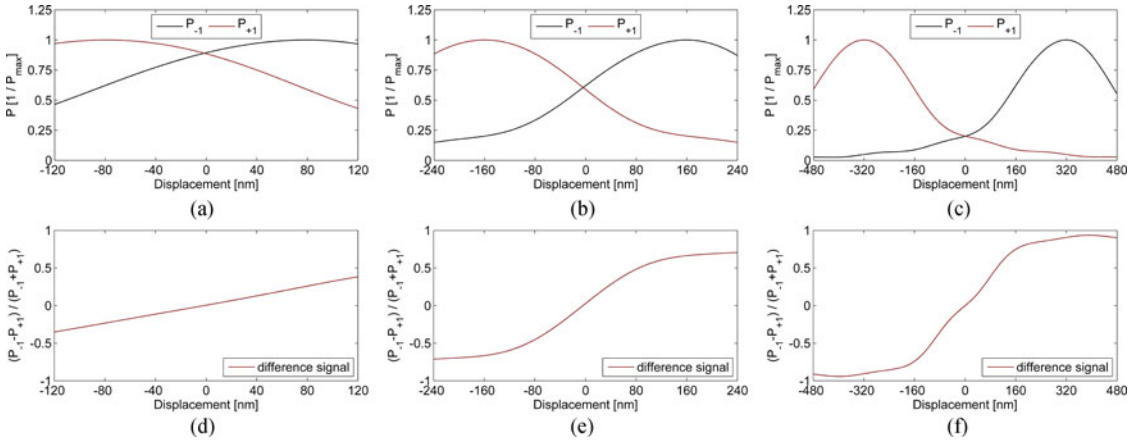

Fig. 12. Comparison of the simulated powers P in the pinholes (a)–(c) and the normalized differences of the sensor output signals S (d)–(f) for the mirror mode Z_1 for different measurement volumes. (a) P 80 nm, (b) P 160 nm, (c) P 320 nm, (d) S 80 nm, (e) S 160 nm, (f) S 320 nm.

significant systematic errors in the optical system have to be known and ideally be compensated in advance.

7. Detailed Analysis of the Measuring Volume

In the presented application, a certain displacement of the ion is related to a certain phase function. Fig. 11 illustrates the effect that an increasing of the defined measurement volume increases the required amplitude of the reference phase front. Therefore, the CGH structure changes. According to [15] the dynamic range of the sensor is limited by the sensor bias, while there is an optimal value for which the sensor sensitivity is the highest. Consequently, there are limitations of the measurement range which can be regarded as the high slope range of the sensor signal. Fig. 12 illustrates the impact of different sensor bias functions on the sensor response. The bias functions of the CGHs correspond to the de-adjustment modes for the de-adjustments of 80 nm, 160 nm, and 320 nm. It can be observed, that the increase in the bias function magnitude (given in terms of ion displacement) decreases the power measured at zero displacement while the measurement range is increased. Due to this limitations, a comparably large measurement volume seems possible only for applications with suitably strong light sources. Low light level induce high sensor noise which results in unreliable data. In any case a simulative evaluation of the sensor response is necessary in order to design a proper sensor for a given application. In the experiments presented before the reliability of simulations was proven. The simulations also expose another limitation of the dynamic range. For increasing sensor bias, the overlapping of the power curves [see Fig. 12(a)–(c)] shrinks. Subsequently, the difference signal S is approaching the sign function (sgn) for which the dynamic

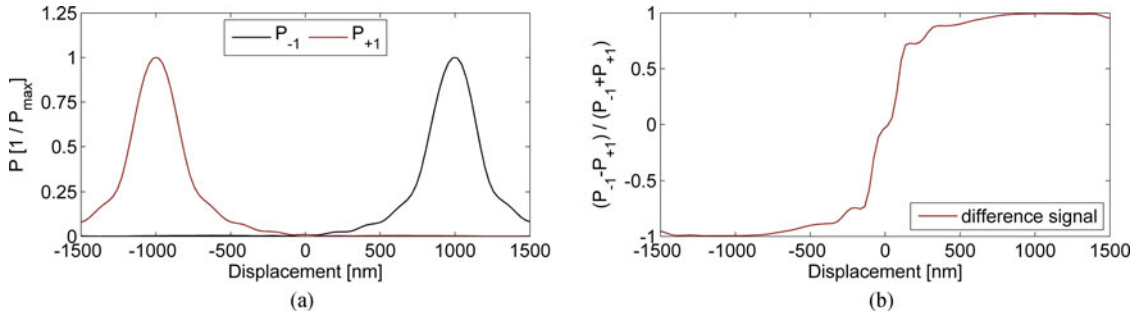

Fig. 13. Comparison of the simulated powers P in the pinholes (a) and the normalized differences of the sensor output signals S (b) for the mirror mode Z_1 for the extreme case (the measurement volume of 1000 nm as half edge length).

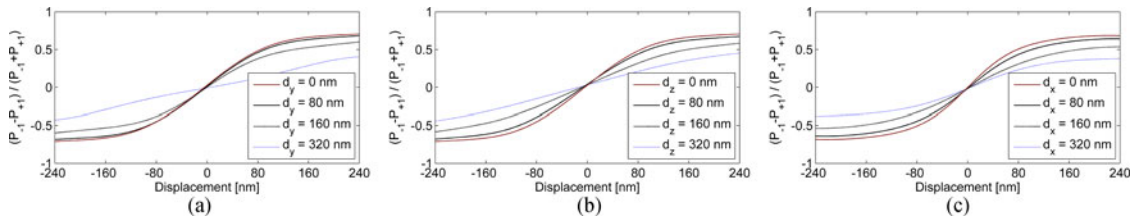

Fig. 14. Simulated sensor response curves of a sensor, designed to detect a misalignment of the light emitter by 160 nm. In the notation **x X y**, x denotes the direction of misalignment which is to be tested and y is an additional misalignment with constant magnitude d_y. The crosstalk between y and all other directions is equivalent to the curves in x-direction. (a) **x X y**. (b) **x X z**. (c) **z X x**.

range equals zero. This trend can already be observed for a sensor bias function corresponding to an ion displacement of 1 μm, as shown in Fig. 13.

8. Intermodal Crosstalk

The influence of a certain mode on the output of a sensor designed to detect another mode is called intermodal crosstalk. As seen before, there are always multiple modes within a real wavefront. The knowledge about modal crosstalk is hence crucial for modal wavefront sensing. The effect of intermodal crosstalk, according to [19], on the sensor output will be discussed in this chapter. For a given area, the optical power on the power sensor depends on the relative magnitudes of all modes contained in the test wavefront and is therefore very complex. Intermodal crosstalk can hinder a proper calibration of the sensor, but there are techniques to reduce the effect on the evaluation level (e.g. in [11], [15], [16]). The sensor response was investigated for the case of an ion which is misaligned in more than one direction. Fig. 14 shows the expected response curves. The notation **x X y** in the plots means, that the evaluation is done for a mode with movement in x-direction, while it is additionally misaligned in the y-direction. The magnitude of misalignment is given in the legend as the length of misalignment from the ideal position. The curves show a significant impact of crosstalk. Nevertheless, the implementation of a closed loop system to find an optimal position for the ion should be possible, once a position close to the focus is found. The response curves flatten with rising magnitude of the disturbing mode. This leads to a subsequent lower sensitivity of the sensor designed for a certain mode.

9. Readout Arrangement

The readout speed of the camera has a great influence on the speed of the measuring process. Accordingly, an improvement in the readout process improves the measurement speed of the overall system. Hence, the arrangement of the PSFs on the detector surface plays a decisive role. Various

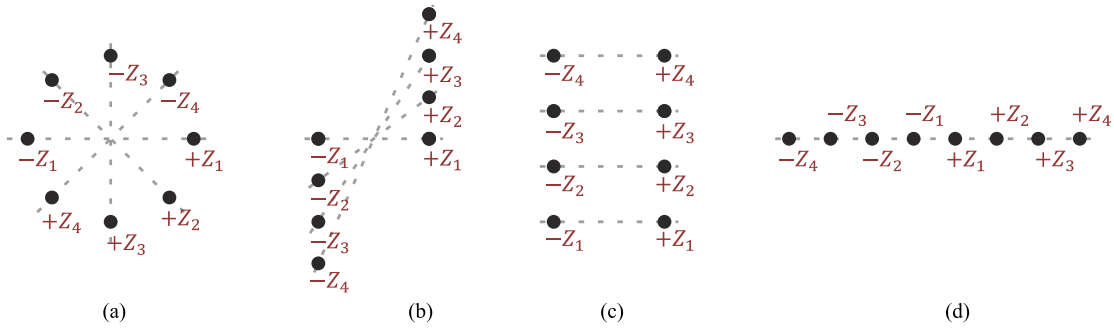

Fig. 15. Possible arrangements of the PSFs of different modes in the ±1st diffraction orders. (a) shows the point-symmetrical, (b) the point symmetrical without rotating, (c) the line-symmetrical, and (d) the line arrangement of the modes which are used. The opposite modes are the same with different signs.

options for this arrangement are possible. The different arrangements have different effects on the sensor speed. By the use of Photodiodes (PDs) or commercial CCD and CMOS based detectors, there are some differences. Fig. 15(a)–(d) shows 4 different sensor arrangements:

a) Every single mode hologram was separated spatially by rotating the tilt function. This arrangement has been discussed and used in various publications and also served as detector arrangement in our application. By placing the pinholes, higher orders do not affect the measurement signal. Through the tilt function the size of the ring can be adjusted to the available detector size.
b) The separation was done via a constant tilt along the local x-axis and a variation of the tilt along the local y-axis. Thus, ±1st diffraction orders are tilted in opposite directions. By this arrangement, only certain columns of the sensor element need to be evaluated, which increases the measuring speed.
c) For this arrangement (as described in [19]), a blazed structure is necessary for each order of each sensor mode. However, this leads to the fact that the individual CGH structures have to be multiplexed in a complex way.
d) By reading only certain lines of the CCD or CMOS chip, the sensor behavior can be improved and the readout speed can be increased. For this arrangement, the use of a line camera can be considered. It should be noted that higher orders of other sensor elements can influence the individual sensor signals significantly as a result of this arrangement.

The use of PDs instead of CCD or CMOS chips actually provides the fastest possible readout speed, but requires a physical set of aperture stops. The set of stops has to be adapted to the readout arrangement. This is not necessary with CCD or CMOS detectors because subsequent image processing is sufficient to adjust the aperture of each detector. By reading out individual lines instead of the entire chip, the sensing speed can be increased by one order of magnitude [20]. The production effort, which involved the design and manufacturing, is the same for arrangement (a), (b), and (d). The arrangements differ only in the adjusted tilt. As already described, the superposition of different orders can lead to disturbance of the measurement. In arrangement (c) especially the fabrication is more difficult to control, because in this arrangement 8 multilevel structures have to be multiplexed.

10. Conclusion

There are different ways to measure the wavefront respectively the wavefront errors of an optical system: the common way is to use Shack-Hartmann Sensors (SHS) that are inpractical in some cases, e.g. in the detection of a fast, fluorescent particle in a definite optical system. Here, the approach of a Modal Wavefront Sensor (MWFS) is very useful [10], [11]. This applies only in the case that either single Photodiodes (PDs) are used as sensor elements (one PD per mode) or if only individual lines (rows or columns) of the 2D sensor chip have to be readout. In contrast to

previous works, this research article describes the application, design, and manufacturing process, as well as the experimental verification of the sensor for a particular application. In principle, a detailed analysis of the effect of different measuring volumes, the intermodal crosstalk (that is mostly discussed in earlier works), and possibilities for the readout arrangement of the PSFs onto the detector plane were presented. As described before, this measurement approach is very useful if the overall system is fully understood and all systematic errors are reproducible. Further steps will include the test with wavefronts which were actually generated by a parabolic mirror as shown in Fig. 1. But not only the use of the sensor in the above-mentioned fundamental research area is possible. The areas of application are also conceivable in biological applications (biological sample measurements). Obviously, the use of the described measuring method has to be adapted to the desired application. Without a priori knowledge of the system to be measured, it does not succeed. The entire sensor must be adapted to the particular application. Through the connection between the MWFS within a closed loop, a reasonable approach can be created.

Acknowledgment

The authors would like to thank the Technology Development and Service Unit (TDSU) 1 (Micro- & Nanostructuring) of the Max Planck Institute for the Science of Light (MPL) for the support during the fabrication of the CGHs.

References

[1] B. C. Platt and R. Shack, "History and principles of Shack-Hartmann wavefront sensing," *J. Refractive Surg.*, vol. 17, no. 5, pp. S573–S577, 2001.
[2] O. G. de Oliveira and D. W. de Lima Monteiro, "Optimization of the Hartmann-Shack microlens array," *Opt. Lasers Eng.*, vol. 49, no. 4, pp. 521–525, 2011.
[3] J. M. Geary, *Introduction to Wavefront Sensors* (SPIE Tutorial Texts in Optical Engineering TT18). Bellingham, WA, USA: SPIE, 1995.
[4] B. R. Brown and A. W. Lohmann, "Complex spatial filtering with binary masks," *Appl. Opt.* vol. 5, no. 6, pp. 967–969, 1966.
[5] D. Malacara, *Optical Shop Testing*. Hoboken, NJ, USA: Wiley, 2007.
[6] C. Liu *et al.*, "Modal wavefront sensor employing stratified computer-generated holographic elements," *Opt. Lasers Eng.*, vol. 51, no. 11, pp. 1265–1271, 2013.
[7] M. A. A. Neil, M. J. Booth, and T. Wilson, "New modal wave-front sensor: A theoretical analysis," *J. Opt. Soc. Amer. A*, vol. 17, no. 6, pp. 1098–1107, 2000.
[8] L. Alber, M. Fischer, M. Bader, K. Mantel, M. Sondermann, and G. Leuchs, "Focusing characteristics of a 4π parabolic mirror light-matter interface," *J. Eur. Opt. Soc. Rapid Publ.*, vol. 13, no. 14, pp. 1–10, 2017.
[9] M. Sondermann and G. Leuchs, "Photon-atom coupling with parabolic mirrors," in *Engineering the Atom-Photon Interaction: Controlling Fundamental Processes With Photons, Atoms and Solids*. Berlin, Germany: Springer, 2015.
[10] S. K. Mishra, R. Bhatt, D. Mohan, A. K. Gupta, and A. Sharma, "Differential modal Zernike wavefront sensor employing a computer-generated hologram: A proposal," *Appl. Opt.*, vol. 48, no. 33, pp. 6458–6465, 2009.
[11] S. Dong *et al.*, "Response analysis of holography-based modal wavefront sensor," *Appl. Opt.*, vol. 51, no. 9, pp. 1318–1327, 2012.
[12] R. Maiwald *et al.*, "Stylus ion trap for enhanced access and sensing," *Nature Phys.*, vol. 5, pp. 551–554, 2009.
[13] J. W. Goodman, *Introduction to Fourier Optics*. New York, NY, USA: McGraw-Hill, 1968.
[14] J. Stehr, F. Loosen, N. Lindlein, and L. Alber, "Design und Herstellung Eines CGH-Basierten Modalen Wellenfrontsensors," in *Proc. 118th Annu. Meeting DGaO*, Dresden, Germany, 2017, pp. 1–2.
[15] M. J. Booth, "Direct measurement of Zernike aberration modes with a modal wavefront sensor," *Proc. SPIE*, vol. 5162, pp. 79–90, 2003.
[16] F. Kong and A. Lambert, "Improvements to the modal holographic wavefront sensor," *Appl. Opt.*, vol. 55, no. 13, pp. 3615–3625, 2016.
[17] I. H. Malitson, "Interspecimen comparison of the refractive index of fused silica," *J. Opt. Soc. Amer.*, vol. 55, no. 10, pp. 1205–1209, 1965.
[18] B. Kress and P. Meyrueis, *Digital Diffractive Optics*. Chicester, U.K.: Wiley, 2000.
[19] F. Ghebremichael, G. P. Andersen, and K. S. Gurley, "Holography-based wavefront sensing," *Appl. Opt.*, vol. 47, no. 4, pp. A62–A69, 2008.
[20] Andor Technol. Ltd., "Zyla–sCMOS–Speed and sensitivity for physical science imaging and spectroscopy," *Tech. Datasheet*, Aug. 2017.